

Imaging heat transport in suspended diamond nanostructures with integrated spin defect thermometers

V. Goblot,^{1,2,*} K. Wu,^{1,3,†} E. Di Lucente,⁴ Y. Zhu,¹ E. Losero,^{1,5} Q. Jobert,¹
C. Jaramillo Concha,¹ N. Marzari,^{4,6} M. Simoncelli,^{7,‡} and C. Galland^{1,2}

¹*Institute of Physics, Swiss Federal Institute of Technology Lausanne (EPFL), CH-1015 Lausanne, Switzerland*

²*Center of Quantum Science and Engineering, Swiss Federal Institute of Technology Lausanne (EPFL), CH-1015 Lausanne, Switzerland*

³*PROUD SA, Lausanne, Switzerland*

⁴*Theory and Simulation of Materials (THEOS), and National Centre for Computational Design and Discovery of Novel Materials (MARVEL), École Polytechnique Fédérale de Lausanne, 1015 Lausanne, Switzerland*

⁵*Istituto Nazionale di Ricerca Metrologica (INRiM), Strada delle Cacce 91, Torino, 10135, Italy*

⁶*Laboratory for Materials Simulations, Paul Scherrer Institut, 5232 Villigen PSI, Switzerland*

⁷*Theory of Condensed Matter Group of the Cavendish Laboratory, University of Cambridge, United Kingdom*

(Dated: November 27, 2024)

Among all materials, mono-crystalline diamond has one of the highest measured thermal conductivities, with values above 2000 W/m/K at room temperature. This stems from momentum-conserving ‘normal’ phonon-phonon scattering processes dominating over momentum-dissipating ‘Umklapp’ processes, a feature that also suggests diamond as an ideal platform to experimentally investigate phonon heat transport phenomena that violate Fourier’s law. Here, we introduce dilute nitrogen-vacancy color centers as in-situ, highly precise spin defect thermometers to image temperature inhomogeneities in single-crystal diamond microstructures heated from ambient conditions. We analyze cantilevers with cross-sections in the range from about 0.2 to 2.6 μm^2 , observing a relation between cross-section and heat flux that departs from Fourier’s law predictions. We rationalize such behavior relying on first-principles simulations based on the linearized phonon Boltzmann transport equation, also discussing how fabrication-induced impurities influence conduction. Our temperature-imaging method can be applied to diamond devices of arbitrary geometry, paving the way for the exploration of unconventional, non-diffusive heat transport phenomena.

Carbon-based materials such as graphene, graphite or diamond present exceptional heat-conduction properties. Due to large phonon group velocities, they exhibit high thermal conductivity – with diamond reaching record values at room temperature and below [1–3]. Moreover, the prevalence of normal (momentum-conserving) phonon-phonon scattering processes over Umklapp (momentum non-conserving) processes in these materials leads to phonon heat transport phenomena that violate Fourier’s law for macroscopic diffusive heat propagation [4]. In graphene and graphite, ballistic transport in nanoscale devices [5, 6] or hydrodynamic heat transport [7–13] have been evidenced at or near room temperature, and recent theoretical work predicted that diamond should also exhibit hydrodynamic heat transport at room temperature [14]. The influence of phonon scattering at grain boundaries has been explored in polycrystalline diamond [15] and unexpected size effects were recently reported in the thermal conductivity of diamond microparticles [16], but experimental data on low-dimensional single-crystal diamond is lacking. Understanding heat transport in nanostructured diamond will be valuable in view of its applications in optomechanics [17, 18], nonlinear optics [19], quantum nanophotonics [20], as well as in heat management devices [21].

A major challenge in the study of thermal transport at the nanoscale is to find appropriate temperature sensors.

Traditional measurements of the heat conductivity rely on resistive sensors combined with advanced sample engineering [5, 11] and cannot provide spatially-resolved temperature measurements. Non contact optical thermometry techniques such as transient thermal gratings [9, 22], and time- or frequency-domain thermoreflectance [23–25] have been widely employed on simple planar geometries but require the deposition of a transducer material, typically a metal [26], and don’t provide a direct temperature readout [27]. Other optical techniques [28, 29], including Raman sideband thermometry [30–33], offer good spatial resolution but rather poor temperature accuracy, typically not better than a few K.

In this work, we use dilute color centers in the diamond lattice as precise in-situ temperature sensors to investigate heat transport properties of suspended diamond microstructures. Diamond hosts optically active spin defects, the most studied being the negatively charged nitrogen vacancy (NV) center [34], which can be used as in-situ nanoscale thermometers [35–37]. Negatively charged NV centers are spin-1 atomic defects formed by a substitutional nitrogen atom neighboring a vacancy in the diamond lattice. Their spin can be initialized and readout by optical pumping and monitoring the photoluminescence intensity. The resonance frequency associated with the transition between $m_s = 0$ and $m_s = \pm 1$ spin states is temperature-dependent [38], as can be tracked with

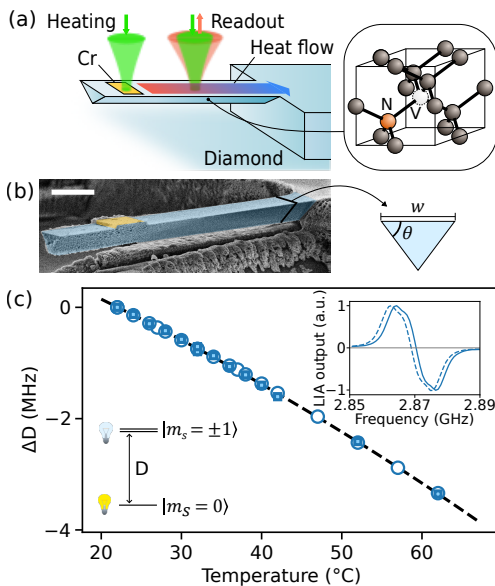


FIG. 1. (a) Schematic representation of the experiment. Right inset: atomic structure of an NV center in the diamond lattice. (b) Scanning electron microscope (SEM) image with false colors for the diamond cantilever (blue) and Cr patch (yellow). Scale bar is 2 μm . Right inset: triangular cantilever cross-section, with width w and angle θ . (c) ZFS shift $\Delta D(T) = D(T) - D(22^\circ\text{C})$ versus bath temperature, measured in bulk diamond (circles) and on a cantilever (squares). Lower inset: Energy levels of the NV center ground state. The “bright” $m_s = 0$ state shows higher photoluminescence than the degenerate, “dark” $m_s = \pm 1$ states, allowing to measure D through ODMR. Top inset: lock-in ODMR spectra measured at 22 $^\circ\text{C}$ (solid line) and 62 $^\circ\text{C}$ (dashed).

either continuous-wave or pulsed optically detected magnetic resonance (ODMR) [39]. NV centers are thus excellent thermometers, offering nanoscale spatial resolution and sub-mK/ $\sqrt{\text{Hz}}$ sensitivity [40] for steady-state temperature measurement near room temperature. Solid-state spin defects acting as temperature sensors are also found in a broad range of materials, including hBN [41], Si [42] and SiC [43–45], making this method widely applicable.

The principle of our experiment is summarized in Fig. 1a. We fabricate suspended micro-cantilevers out of single crystal diamond grown by chemical vapour deposition and enriched in ^{12}C ($> 99.95\%$), containing NV centers up to a concentration of 3 ppm. Cantilevers are patterned using electron-beam lithography and subsequent etching, in two steps: first a step of vertical, oxygen-based reactive ion etching, followed by focused ion beam (FIB) milling at an angle $\theta = 53^\circ$ from the diamond surface. This results in triangular cantilever cross-sections, as visible in Fig. 1b. The cantilever acts as a one-dimensional channel for heat transport. A small chromium patch is added at the cantilever tip to serve as a heat source upon absorption of a 515 nm laser fo-

cused onto it (referred to as heating laser) and the bulk diamond acts as a heat sink. In the future, a UV-C laser could be used to heat diamond directly, as shown in other wide-gap materials [33]. Complete details on the sample fabrication can be found in the Supplementary Material (SM) [46].

Photoluminescence from NV centers is collected in confocal geometry, using a second 515 nm laser beam to address a large ensemble of NV centers (about 10^5) located in the diffraction-limited spot. This second laser is referred to as readout laser. The temperature-dependent zero-field splitting (ZFS) between $m_s = 0$ and $m_s = \pm 1$ states is measured through continuous wave (cw) ODMR. We use a lock-in amplifier (LIA) combined with frequency modulation of the microwave to achieve high signal to noise ratio [47]. The absolute value of the ZFS is found to depend on position [46], possibly due to the presence of local strain. Since our cantilevers are free-standing, we do not expect that heating induces any additional strain (except maybe very near its base). We measure the change of ZFS against a reference temperature and present in Fig. 1c the results for bulk diamond and a cantilever. Our data is fitted by the model from Ref. [48], with only two fitting parameters (dashed line in Fig. 1c).

The calibration is used to convert values of ZFS shift to local temperature under the readout laser spot. Noise analysis gives a typical temperature sensitivity of 0.27 K/ $\sqrt{\text{Hz}}$ for the temperature readout on the cantilever [46]. The choice of cw-ODMR is a trade-off between sensitivity requirement and simplicity of experimental implementation. Even though more sophisticated NV-based thermometry schemes allow to reach better sensitivity, relying e.g. on pulse sequences [35, 36] or on multi-frequency drive [40], the dominant sources of uncertainties in our case come from the estimates of absorbed laser power and cantilever cross-section, as detailed below.

The heating laser is used to induce a heat flow in a cantilever. Fig. 2a presents the measured local temperature rise ΔT as a function of heating laser power P_h , for a readout spot located at a fixed position in the middle of the cantilever. We observe a linear relation between ΔT and heating power. Standard deviations of residuals after a linear fit give a temperature error of ± 0.25 K [46]. This value includes systematic errors due e.g to imperfect alignment of the heating laser on the gold patch, explaining why it is slightly higher than the readout error (± 0.15 K with our 3 s integration time).

Fixing the heating laser power, we measure the space-dependent temperature profile along the cantilever by sweeping the position of the readout laser. For each readout laser position, the ZFS values are measured without and with heating. To illustrate the method, the temperature profile for a cantilever of varying width is shown in Fig. 2b-c. A section of constant width shows

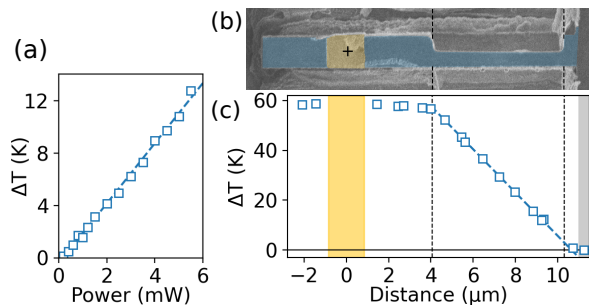


FIG. 2. (a) Temperature shift ΔT at a fixed readout position on the cantilever versus heating laser power P_h . Dashed line is a linear fit. (b) SEM image (top view) of a $1.53 \mu\text{m}$ -wide cantilever (blue) with a narrow section ($0.73 \mu\text{m}$) between the Cr patch (yellow) and the bulk, as indicated by the vertical dashed lines. The black cross indicates the heating laser position. (c) Temperature profile measured along the cantilever at $P_h = 3.0 \text{ mW}$, by sweeping the position x of the readout laser. The dashed line is a linear fit of $\Delta T(x)$ in the narrow section.

linear temperature profile and the narrow section has a much steeper temperature gradient than the wide section, while the temperature is constant on the free-hanging side. In our experimental setting, the spatial resolution is diffraction-limited, the readout laser spot size being $\sim 0.44 \mu\text{m}$ in diameter.

We can consider the case of standard diffusive heat transport to develop a picture of the expected behavior: According to Fourier’s law, in 1D, $q = -\kappa \partial T / \partial x$, with q the local heat flux density and κ the material’s thermal conductivity, which depends slowly on temperature. We confirmed that the Cr patch’s temperature remains close to that of the underlying diamond [46], so that convective and radiative thermal losses can be neglected. In this case, $q = \alpha P_h / S$, with P_h the heating laser power incident on the Cr patch, α the Cr patch absorption coefficient and $S = \tan(\theta) w^2 / 4$ the cantilever cross-section. For small ΔT , Fourier’s law predicts a linear temperature profile along the cantilever, compatible with the results from Fig. 2. However, having a linear temperature profile is a necessary but not sufficient condition for the validity of Fourier’s law, since it also assumes thermal conductivity to be an intrinsic, size-independent material’s property, and consequently predicts a heat flux that scales linearly with the cantilever cross-section. Instead, in diamond, κ has been predicted to decrease to approximately half of its bulk value at widths $\sim 0.7 \mu\text{m}$ [49, 50] – a much stronger reduction than other materials for this channel size [51–55]. We now show that a reduction of κ is observed when reducing the lateral size of the cantilever.

We investigate cantilevers with different lateral width w , in the range 0.8 - $2.5 \mu\text{m}$, and identical length of $10 \mu\text{m}$. The lower bound of this range originates from limitations in temperature sensitivity for cantilever widths below the

diffraction limited spot size (due to the reduced number of probed NV centers). Conversely, the upper bound is due to the difficulty in fabricating suspended cantilevers with dimensions bigger than $3 \mu\text{m}$ (due to the long etching time required). We measure the temperature profile along each individual cantilever, adjusting P_h such that the maximum temperature rise is comparable in all cases and remains below 40 K . The results are presented in Fig. 3, with panel (c) presenting the measured temperature gradient $\partial T / \partial x$, normalized by P_h , versus cantilever width w . In the case of purely diffusive thermal transport, Fourier law predicts that this normalized temperature gradient is inversely proportional to the cantilevers cross-section. Specifically, since all our cantilevers have triangular cross-section with same angle θ , Fourier’s law predicts $\partial T / \partial x \propto w^{-2}$. In contrast, our experiments deviate from this prediction, with a temperature gradient displaying a scaling approximately proportional to w^{-3} for $w < 2 \mu\text{m}$.

We model thermal transport in our cantilevers using the viscous heat equations (VHE), two coupled mesoscopic heat-transport equations for temperature and phonon drift velocity [14] that generalize Fourier’s laws encompassing not only heat diffusion but also fluid-like behavior [9–12, 56]. The VHE can be parametrized from first principles and allow to describe how microstructured geometries influence thermal transport with accuracy comparable to microscopic models based on the full space-dependent solution of the linearized Boltzmann transport equation (LBTE) [57, 58], at much reduced computational cost [59]. Therefore, we employ the VHE to investigate how the geometry of our cantilevers affects thermal transport, and we assess the relevance of viscous effects by comparing the VHE predictions with those obtained from Fourier’s law.

We simulate the three-dimensional experimental geometry, imposing a temperature gradient $\Delta T = 10 \text{ K}$ around room temperature on $L = 10 \mu\text{m}$ long cantilevers. Parameters entering in the VHE or Fourier’s law are computed from first-principles, accounting for third-order anharmonic phonon-phonon scattering [50, 60], phonon-impurity scattering [61], as well as for the effects of rough cantilever’s boundaries [49] (see SM [46] for details). Then, we solve the VHE or Fourier’s law and determine the heat flux \mathbf{q} from their solution. Finally, we evaluate the effective thermal conductivity as $\kappa_{\text{eff}} = \frac{L}{\Delta T} [S^{-1} \iint_S \mathbf{q} \cdot d\mathbf{S}]$, where S is the cantilever cross section, and $d\mathbf{S}$ the oriented surface element.

In Fig. 4 we compare the experimental values for κ_{eff} , extracted from the measurements in Fig. 3 (see SM [46] for details), against predictions obtained solving the VHE or Fourier’s law. In the numerical simulations, we consider two different impurity scenarios to compute transport coefficients from first principles. First, we consider the ideal case of pristine diamond cantilevers with only 0.05% ^{13}C isotopes (dashed lines). In this idealized case,

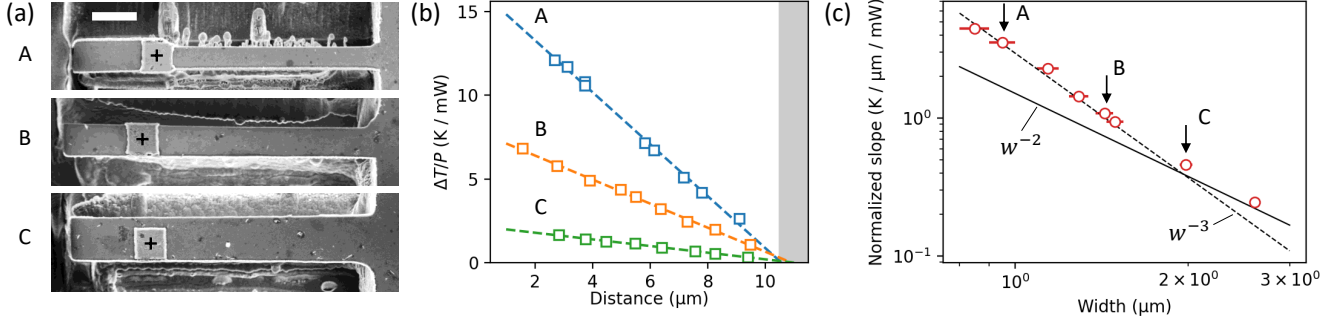


FIG. 3. (a) SEM images, top view of cantilevers with width: $w = 0.95 \mu\text{m}$ (A), $1.43 \mu\text{m}$ (B) and $1.98 \mu\text{m}$ (C). Black cross indicates the heating laser position, corresponding to $x = 0$ in (b). (b) Temperature profile measured in corresponding cantilevers, normalized by applied heating power P_h . (c) Normalized temperature gradient extracted from profiles in (b) versus cantilever width w . Solid and lines are a guide for the eye, corresponding to the w^{-2} scaling predicted by Fourier’s law, and the w^{-3} scaling observed for $w < 2 \mu\text{m}$.

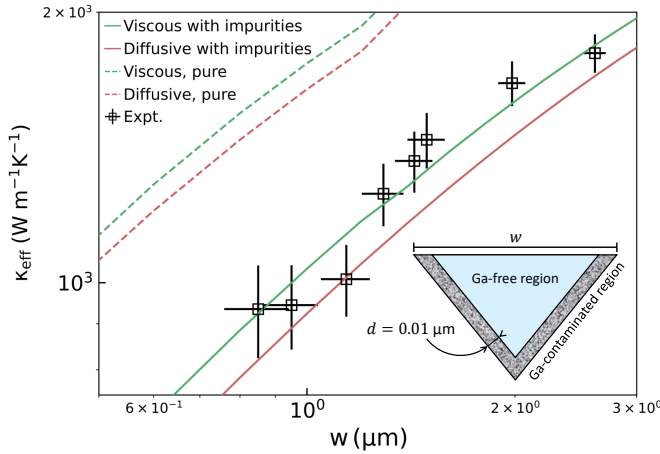


FIG. 4. Effective thermal conductivity of diamond cantilevers as a function of width w . Black squares are experiments, with error bars accounting for uncertainties on width and temperature gradient. Lines are first-principles predictions based on the viscous heat equations (green) or Fourier’s law (red); results that account for Ga impurities introduced during fabrication and with concentration proportional to the surface-to-volume ratio (see text) are solid, while predictions that consider impurity scattering only from carbon isotopes (0.05% of ^{13}C) are dashed. Inset, cantilever cross-section with Ga impurities in proximity of the milled surfaces (penetration depth $0.01 \mu\text{m}$). The top surface is protected with a Ti layer during fabrication, hence not contaminated.

the VHE and Fourier’s law yield κ_{eff} values having minor differences; however, both are significantly higher than the experimental values.

To address this discrepancy, we investigate theoretically the effect of additional sources of thermal resistance missing from simulations of pristine samples. In particular, FIB milling is known to cause contamination by Ga ions [62] (Fig. 4 inset) that can be as high as hundreds of ppm within a penetration depth that we estimate to be

$d = 0.01 \mu\text{m}$ [46]. This penetration layer is expected to be the same for all cantilevers since we used the same FIB parameters. Consequently, Ga contamination is expected to have an increasing impact on thermal conductivity as the cantilever width w decreases. We account for the influence of Ga impurities using the model of Ref. [61], considering an average concentration of Ga impurities proportional to the surface-to-volume ratio, and determine a single parameter η_{Ga} — the concentration of Ga impurities in the penetration layer — from a fit to the experimental data [46].

Solid lines in Fig. 4 are the calculated values for κ_{eff} within this one-parameter model, where the concentration of Ga impurities in the penetration layer obtained from the fit is $\eta_{\text{Ga}} = 213 \text{ ppm}$ (a value of the same order of magnitude as those in Ref. [62]). Nitrogen and vacancy impurities are also present in the diamond with concentrations of the order of 10 ppm, which is expected to have a comparatively negligible effect on thermal conductivity [63]. A model with constant concentration of impurities over the whole cross-section fails to reproduce the experiments, especially in the steepness of the reduction of κ_{eff} with decreasing w [46]. This suggests that the main hypothesis of our model — having average concentration of Ga impurities proportional to the surface-to-volume ratio of the cantilevers — is realistic and captures the most important microscopic physics. Finally, hydrodynamic effects (quantified by the difference between green and red curves) appear practically unimportant and the deviation from Fourier’s law are mainly caused by κ_{eff} being not an intrinsic property but a size-dependent quantity.

In conclusion, we highlight that this experimental platform consisting of NV centers in diamond nanostructures offers multiple routes for new investigations. First, the question arises of how to maximize heat conductivity in sub-micrometer diamond channels, which can be an-

swered by achieving a finer control on the impurity levels. The effect of sidewall roughness on phonon scattering at the boundaries [64, 65] can also be probed by varying the etching method and chemical termination of the diamond surface. Second, hydrodynamic effects in heat transport could be revealed using refined geometries that enhance unambiguous signatures of hydrodynamic features, such as heat vortices [59]. Third, this research can be pushed toward even smaller channels to address open questions in quantized phononic heat conductance [66]. Overall, our results demonstrate the potential of solid state spin defects in ultrahigh thermal conductivity materials to explore heat transport phenomena in non-Fourier regimes.

Acknowledgments. This project has received funding from the Swiss National Science Foundation through grant 198898 and 216406, EPFL Center for Quantum Science and Engineering through a Collaborative Research Fellowship, the European Union’s Horizon 2020 research and innovation programmes under the Marie Skłodowska-Curie grant agreement 945363 and under grant agreement 101112347, Project NerveRepack. M. S. acknowledges support from: (i) the Kelvin2 HPC platform at the NI-HPC Centre (funded by EPSRC and jointly managed by Queen’s University Belfast and Ulster University); (ii) the UK National Supercomputing Service ARCHER2, for which access was obtained via the UKCP consortium and funded by EPSRC [EP/X035891/1]; (iii) Gonville and Caius College. N.M and E.D. acknowledge support from the Swiss National Science Foundation (SNSF), through Grant No. CR-SII5.189924 (“Hydronics” project). The diamond cantilevers were fabricated at the EPFL Center of Micro-NanoTechnology (CMi) and we gratefully acknowledge the support of EPFL CMi.

* Contact author: valentin.goblot@epfl.ch

† These authors contributed equally to this work.

‡ Contact author: ms2855@cam.ac.uk

- [1] R. Berman, P. R. W. Hudson, and M. Martinez, Nitrogen in diamond: evidence from thermal conductivity, *Journal of Physics C: Solid State Physics* **8**, L430 (1975).
- [2] J. R. Olson, R. O. Pohl, J. W. Vandersande, A. Zoltan, T. R. Anthony, and W. F. Banholzer, Thermal conductivity of diamond between 170 and 1200 k and the isotope effect, *Phys. Rev. B* **47**, 14850 (1993).
- [3] A. V. Inyushkin, A. N. Taldenkov, V. G. Ralchenko, A. P. Bolshakov, A. V. Koliadin, and A. N. Katrusha, Thermal conductivity of high purity synthetic single crystal diamonds, *Phys. Rev. B* **97**, 144305 (2018).
- [4] G. Chen, Non-fourier phonon heat conduction at the microscale and nanoscale, *Nature Reviews Physics* , 1 (2021).
- [5] M.-H. Bae, Z. Li, Z. Aksamija, P. N. Martin, F. Xiong, Z.-Y. Ong, I. Knezevic, and E. Pop, Ballistic to diffusive crossover of heat flow in graphene ribbons, *Nature Communications* **4**, 1734 (2013).
- [6] D. L. Nika and A. A. Balandin, Two-dimensional phonon transport in graphene, *Journal of Physics: Condensed Matter* **24**, 233203 (2012).
- [7] A. Cepellotti, G. Fugallo, L. Paulatto, M. Lazzeri, F. Mauri, and N. Marzari, Phonon hydrodynamics in two-dimensional materials, *Nature communications* **6**, 6400 (2015).
- [8] S. Lee, D. Broido, K. Esfarjani, and G. Chen, Hydrodynamic phonon transport in suspended graphene, *Nature Communications* **6**, 6290 (2015).
- [9] S. Huberman, R. A. Duncan, K. Chen, B. Song, V. Chiloyan, Z. Ding, A. A. Maznev, G. Chen, and K. A. Nelson, Observation of second sound in graphite at temperatures above 100 k, *Science* **364**, 375 (2019).
- [10] Z. Ding, K. Chen, B. Song, J. Shin, A. A. Maznev, K. A. Nelson, and G. Chen, Observation of second sound in graphite over 200 k, *Nature Communications* **13**, 285 (2022).
- [11] Y. Machida, N. Matsumoto, T. Isono, and K. Behnia, Phonon hydrodynamics and ultrahigh-room-temperature thermal conductivity in thin graphite, *Science* **367**, 309 (2020).
- [12] J. Jeong, X. Li, S. Lee, L. Shi, and Y. Wang, Transient hydrodynamic lattice cooling by picosecond laser irradiation of graphite, *Phys. Rev. Lett.* **127**, 085901 (2021).
- [13] X. Huang, Y. Guo, Y. Wu, S. Masubuchi, K. Watanabe, T. Taniguchi, Z. Zhang, S. Volz, T. Machida, and M. Nomura, Observation of phonon poiseuille flow in isotopically purified graphite ribbons, *Nature Communications* **14**, 2044 (2023).
- [14] M. Simoncelli, N. Marzari, and A. Cepellotti, Generalization of fourier’s law into viscous heat equations, *Phys. Rev. X* **10**, 011019 (2020).
- [15] A. Sood, R. Cheaito, T. Bai, H. Kwon, Y. Wang, C. Li, L. Yates, T. Bougher, S. Graham, M. Asheghi, M. Goorsky, and K. E. Goodson, Direct Visualization of Thermal Conductivity Suppression Due to Enhanced Phonon Scattering Near Individual Grain Boundaries, *Nano Letters* **18**, 3466 (2018).
- [16] Y. Wang and B. Sun, Anomalously strong size effect on thermal conductivity of diamond microparticles, *Applied Physics Letters* **125**, 042202 (2024).
- [17] Y. Tao, J. M. Boss, B. A. Moores, and C. L. Degen, Single-crystal diamond nanomechanical resonators with quality factors exceeding one million, *Nature Communications* **5**, 3638 (2014).
- [18] M. Mitchell, B. Khanaliloo, D. P. Lake, T. Masuda, J. P. Hadden, and P. E. Barclay, Single-crystal diamond low-dissipation cavity optomechanics, *Optica* **3**, 963 (2016).
- [19] B. J. M. Hausmann, I. Bulu, V. Venkataraman, P. Deotare, and M. Lončar, Diamond nonlinear photonics, *Nature Photon* **8**, 369 (2014).
- [20] G. Moody, V. J. Sorger, D. J. Blumenthal, P. W. Juodawlkis, W. Loh, C. Sorace-Agaskar, A. E. Jones, K. C. Balram, J. C. F. Matthews, A. Laing, M. Davanco, L. Chang, J. E. Bowers, N. Quack, C. Galland, I. Aharonovich, M. A. Wolff, C. Schuck, N. Sinclair, M. Lončar, T. Komljenovic, D. Weld, S. Mookherjee, S. Buckley, M. Radulaski, S. Reitzenstein, B. Pingault, B. Machielse, D. Mukhopadhyay, A. Akimov, A. Zheltikov, G. S. Agarwal, K. Srinivasan, J. Lu, H. X.

- Tang, W. Jiang, T. P. McKenna, A. H. Safavi-Naeini, S. Steinhauer, A. W. Elshaari, V. Zwiller, P. S. Davids, N. Martinez, M. Gehl, J. Chiaverini, K. K. Mehta, J. Romero, N. B. Lingaraju, A. M. Weiner, D. Peace, R. Cernansky, M. Lobino, E. Diamanti, L. T. Vidarte, and R. M. Camacho, 2022 roadmap on integrated quantum photonics, *Journal of Physics: Photonics* **4**, 012501 (2022).
- [21] X. Liu, G. Zhang, and Y.-W. Zhang, Surface-engineered nanoscale diamond films enable remarkable enhancement in thermal conductivity and anisotropy, *Carbon* **94**, 760 (2015).
- [22] A. J. Minnich, J. A. Johnson, A. J. Schmidt, K. Esfarjani, M. S. Dresselhaus, K. A. Nelson, and G. Chen, Thermal conductivity spectroscopy technique to measure phonon mean free paths, *Phys. Rev. Lett.* **107**, 095901 (2011).
- [23] K. T. Regner, D. P. Sellan, Z. Su, C. H. Amon, A. J. H. McGaughey, and J. A. Malen, Broadband phonon mean free path contributions to thermal conductivity measured using frequency domain thermoreflectance, *Nature Communications* **4**, 1640 (2013).
- [24] Y. Hu, L. Zeng, A. J. Minnich, M. S. Dresselhaus, and G. Chen, Spectral mapping of thermal conductivity through nanoscale ballistic transport, *Nature Nanotechnology* **10**, 701 (2015).
- [25] F. Tian, B. Song, X. Chen, N. K. Ravichandran, Y. Lv, K. Chen, S. Sullivan, J. Kim, Y. Zhou, T.-H. Liu, M. Goni, Z. Ding, J. Sun, G. A. G. Udalamatta Gamage, H. Sun, H. Ziyadee, S. Huyan, L. Deng, J. Zhou, A. J. Schmidt, S. Chen, C.-W. Chu, P. Y. Huang, D. Broido, L. Shi, G. Chen, and Z. Ren, Unusual high thermal conductivity in boron arsenide bulk crystals, *Science* **361**, 582 (2018).
- [26] R. Wilson, B. A. Apgar, L. W. Martin, and D. G. Cahill, Thermoreflectance of metal transducers for optical pump-probe studies of thermal properties, *Optics express* **20**, 28829 (2012).
- [27] X. Huang, R. Anufriev, L. Jalabert, K. Watanabe, T. Taniguchi, Y. Guo, Y. Ni, S. Volz, and M. Nomura, A graphite thermal tesla valve driven by hydrodynamic phonon transport, *Nature*, 1 (2024).
- [28] C. D. S. Brites, P. P. Lima, N. J. O. Silva, A. Millán, V. S. Amaral, F. Palacio, and L. D. Carlos, Thermometry at the nanoscale, *Nanoscale* **4**, 4799 (2012).
- [29] M. Quintanilla and L. M. Liz-Marzán, Guiding Rules for Selecting a Nanothermometer, *Nano Today* **19**, 126 (2018).
- [30] A. A. Balandin, S. Ghosh, W. Bao, I. Calizo, D. Teweldebrhan, F. Miao, and C. N. Lau, Superior Thermal Conductivity of Single-Layer Graphene, *Nano Letters* **8**, 902 (2008).
- [31] S. Ghosh, I. Calizo, D. Teweldebrhan, E. P. Pokatilov, D. L. Nika, A. A. Balandin, W. Bao, F. Miao, and C. N. Lau, Extremely high thermal conductivity of graphene: Prospects for thermal management applications in nanoelectronic circuits, *Applied Physics Letters* **92**, 151911 (2008).
- [32] O. Braun, R. Furrer, P. Butti, K. Thodkar, I. Shorubalko, I. Zardo, M. Calame, and M. L. Perrin, Spatially mapping thermal transport in graphene by an opto-thermal method, *npj 2D Materials and Applications* **6**, 1 (2022).
- [33] M. Elhajhasan, W. Seemann, K. Dudde, D. Vaske, G. Callsen, I. Rousseau, T. F. Weatherley, J.-F. Carlin, R. Butté, N. Grandjean, *et al.*, Optical and thermal characterization of a group-iii nitride semiconductor membrane by microphotoluminescence spectroscopy and raman thermometry, *Physical Review B* **108**, 235313 (2023).
- [34] M. W. Doherty, N. B. Manson, P. Delaney, F. Jelezko, J. Wrachtrup, and L. C. L. Hollenberg, The nitrogen-vacancy colour centre in diamond, *Physics Reports* **528**, 1 (2013).
- [35] P. Neumann, I. Jakobi, F. Dolde, C. Burk, R. Reuter, G. Waldherr, J. Honert, T. Wolf, A. Brunner, J. H. Shim, D. Suter, H. Sumiya, J. Isoya, and J. Wrachtrup, High-precision nanoscale temperature sensing using single defects in diamond, *Nano Letters* **13**, 2738 (2013).
- [36] D. M. Toyli, C. F. d. l. Casas, D. J. Christle, V. V. Dobrovitski, and D. D. Awschalom, Fluorescence thermometry enhanced by the quantum coherence of single spins in diamond, *Proceedings of the National Academy of Sciences* **110**, 8417 (2013).
- [37] G. Kucsko, P. C. Maurer, N. Y. Yao, M. Kubo, H. J. Noh, P. K. Lo, H. Park, and M. D. Lukin, Nanometre-scale thermometry in a living cell, *Nature* **500**, 54 (2013).
- [38] V. M. Acosta, E. Bauch, M. P. Ledbetter, A. Waxman, L.-S. Bouchard, and D. Budker, Temperature dependence of the nitrogen-vacancy magnetic resonance in diamond, *Physical Review Letters* **104**, 070801 (2013).
- [39] J. F. Barry, J. M. Schloss, E. Bauch, M. J. Turner, C. A. Hart, L. M. Pham, and R. L. Walsworth, Sensitivity optimization for nv-diamond magnetometry, *Rev. Mod. Phys.* **92**, 015004 (2020).
- [40] A. M. Wojciechowski, M. Karadas, C. Osterkamp, S. Jankuhn, J. Meijer, F. Jelezko, A. Huck, and U. L. Andersen, Precision temperature sensing in the presence of magnetic field noise and vice-versa using nitrogen-vacancy centers in diamond, *Applied Physics Letters* **113**, 013502 (2018).
- [41] A. Gottscholl, M. Diez, V. Soltamov, C. Kasper, D. Krauß, A. Sperlich, M. Kianinia, C. Bradac, I. Aharonovich, and V. Dyakonov, Spin defects in hBN as promising temperature, pressure and magnetic field quantum sensors, *Nature Communications* **12**, 4480 (2021).
- [42] C. Beaufils, W. Redjem, E. Rousseau, V. Jacques, A. Y. Kuznetsov, C. Raynaud, C. Voisin, A. Benali, T. Herzig, S. Pezzagna, J. Meijer, M. Abbarchi, and G. Cassabois, Optical properties of an ensemble of g-centers in silicon, *Physical Review B* **97**, 035303 (2018).
- [43] H. Kraus, V. A. Soltamov, F. Fuchs, D. Simin, A. Sperlich, P. G. Baranov, G. V. Astakhov, and V. Dyakonov, Magnetic field and temperature sensing with atomic-scale spin defects in silicon carbide, *Scientific Reports* **4**, 5303 (2014).
- [44] A. N. Anisimov, D. Simin, V. A. Soltamov, S. P. Lebedev, P. G. Baranov, G. V. Astakhov, and V. Dyakonov, Optical thermometry based on level anticrossing in silicon carbide, *Scientific Reports* **6**, 33301 (2016).
- [45] Y. Zhou, J. Wang, X. Zhang, K. Li, J. Cai, and W. Gao, Self-protected thermometry with infrared photons and defect spins in silicon carbide, *Physical Review Applied* **8**, 044015 (2017).
- [46] See Supplemental Material at ... for further details on experimental and theoretical methods and additional data.
- [47] S.-C. Zhang, Y. Dong, B. Du, H.-B. Lin, S. Li, W. Zhu, G.-Z. Wang, X.-D. Chen, G.-C. Guo, and F.-W. Sun, A robust fiber-based quantum thermometer coupled with

- nitrogen-vacancy centers, *Review of Scientific Instruments* **92**, 044904 (2021).
- [48] M. C. Cambria, G. Thiering, A. Norambuena, H. T. Dinani, A. Gardill, I. Kemeny, V. Lordi, A. Gali, J. R. Maze, and S. Kolkowitz, Physically motivated analytical expression for the temperature dependence of the zero-field splitting of the nitrogen-vacancy center in diamond, *Phys. Rev. B* **108**, L180102 (2023).
- [49] W. Li, N. Mingo, L. Lindsay, D. A. Broido, D. A. Stewart, and N. A. Katcho, Thermal conductivity of diamond nanowires from first principles, *Physical Review B—Condensed Matter and Materials Physics* **85**, 195436 (2012).
- [50] G. Fugallo, M. Lazzeri, L. Paulatto, and F. Mauri, *Ab initio* variational approach for evaluating lattice thermal conductivity, *Phys. Rev. B* **88**, 045430 (2013).
- [51] M. v. Swinkels, M. Van Delft, D. Oliveira, A. Cavalli, I. v. Zardo, R. Van Der Heijden, and E. Bakkers, Diameter dependence of the thermal conductivity of inas nanowires, *Nanotechnology* **26**, 385401 (2015).
- [52] P. Martin, Z. Aksamija, E. Pop, and U. Ravaioli, Impact of phonon-surface roughness scattering on thermal conductivity of thin si nanowires, *Physical review letters* **102**, 125503 (2009).
- [53] A. I. Hochbaum, R. Chen, R. D. Delgado, W. Liang, E. C. Garnett, M. Najarian, A. Majumdar, and P. Yang, Enhanced thermoelectric performance of rough silicon nanowires, *Nature* **451**, 163 (2008).
- [54] D. Li, Y. Wu, P. Kim, L. Shi, P. Yang, and A. Majumdar, Thermal conductivity of individual silicon nanowires, *Applied Physics Letters* **83**, 2934 (2003).
- [55] J. Maire, R. Anufriev, and M. Nomura, Ballistic thermal transport in silicon nanowires, *Scientific Reports* **7**, 41794 (2017).
- [56] M. Gandolfi, C. Giannetti, and F. Banfi, Temperonic crystal: A superlattice for temperature waves in graphene, *Phys. Rev. Lett.* **125**, 265901 (2020).
- [57] M. Raya-Moreno, X. Cartoixà, and J. Carrete, BTE-Barna: An extension of almaBTE for thermal simulation of devices based on 2D materials, *Computer Physics Communications* **281**, 108504 (2022).
- [58] M. Raya-Moreno, J. Carrete, and X. Cartoixà, Hydrodynamic signatures in thermal transport in devices based on two-dimensional materials: An *ab initio* study, *Physical Review B* **106**, 014308 (2022).
- [59] J. Dragašević and M. Simoncelli, Viscous heat backflow and temperature resonances in extreme thermal conductors (2024), arXiv:2303.12777 [cond-mat.mtrl-sci].
- [60] W. Li, J. Carrete, N. A. Katcho, and N. Mingo, Shengbte: A solver of the boltzmann transport equation for phonons, *Computer Physics Communications* **185**, 1747 (2014).
- [61] C. Ratsifaritana and P. Klemens, Scattering of phonons by vacancies, *International journal of thermophysics* **8**, 737 (1987).
- [62] I. Bayn, A. Bolker, C. Cytermann, B. Meyler, V. Richter, J. Salzman, and R. Kalish, Diamond processing by focused ion beam—surface damage and recovery, *Applied Physics Letters* **99**, 183109 (2011).
- [63] N. A. Katcho, J. Carrete, W. Li, and N. Mingo, Effect of nitrogen and vacancy defects on the thermal conductivity of diamond: An *ab initio* green’s function approach, *Phys. Rev. B* **90**, 094117 (2014).
- [64] T. R. Anthony, J. L. Fleischer, J. R. Olson, and D. G. Cahill, The thermal conductivity of isotopically enriched polycrystalline diamond films, *Journal of Applied Physics* **69**, 8122 (1991).
- [65] S. Tian, T. Wang, H. Chen, D. Ma, and L. Zhang, Phonon coherent transport leads to an anomalous boundary effect on the thermal conductivity of a rough graphene nanoribbon, *Phys. Rev. Appl.* **21**, 064005 (2024).
- [66] C. A. Polanco, A. van Roekeghem, B. Brisuda, L. Saminadayar, O. Bourgeois, and N. Mingo, The phonon quantum of thermal conductance: Are simulations and measurements estimating the same quantity?, *Science Advances* **9**, eadi7439 (2023).
- [67] R. Chambers, The conductivity of thin wires in a magnetic field, *Proceedings of the Royal Society of London. Series A. Mathematical and Physical Sciences* **202**, 378 (1950).
- [68] J. M. Ziman, *Electrons and phonons: the theory of transport phenomena in solids* (Oxford university press, 2001).
- [69] S. Mi, A. Toros, T. Graziosi, and N. Quack, Non-contact polishing of single crystal diamond by ion beam etching, *Diamond and Related Materials* **92**, 248 (2019).
- [70] M. J. Burek, Y. Chu, M. S. Z. Liddy, P. Patel, J. Rochman, S. Meesala, W. Hong, Q. Quan, M. D. Lukin, and M. Lončar, High quality-factor optical nanocavities in bulk single-crystal diamond, *Nature Communications* **5**, 5718 (2014).
- [71] T. Graziosi, S. Mi, M. Kiss, and N. Quack, Single crystal diamond micro-disk resonators by focused ion beam milling, *Apl Photonics* **3** (2018).
- [72] J. Riedrich-Möller, L. Kipfstuhl, C. Hepp, E. Neu, C. Pauly, F. Mücklich, A. Baur, M. Wandt, S. Wolff, M. Fischer, S. Gsell, M. Schreck, and C. Becher, One- and two-dimensional photonic crystal microcavities in single crystal diamond, *Nature Nanotechnology* **7**, 69 (2012).
- [73] Y.-Y. Cai, E. Sung, R. Zhang, L. J. Tauzin, J. G. Liu, B. Ostovar, Y. Zhang, W.-S. Chang, P. Nordlander, and S. Link, Anti-stokes emission from hot carriers in gold nanorods, *Nano Letters* **19**, 1067 (2019), publisher: American Chemical Society.
- [74] A. Carattino, M. Caldarola, and M. Orrit, Gold Nanoparticles as Absolute Nanothermometers, *Nano Letters* **18**, 874 (2018).
- [75] T. Jollans, M. Caldarola, Y. Sivan, and M. Orrit, Effective Electron Temperature Measurement Using Time-Resolved Anti-Stokes Photoluminescence, *The Journal of Physical Chemistry A* **124**, 6968 (2020).
- [76] K. T. Crampton, A. Fast, E. O. Potma, and V. A. Apkarian, Junction Plasmon Driven Population Inversion of Molecular Vibrations: A Picosecond Surface-Enhanced Raman Spectroscopy Study, *Nano Letters* **18**, 5791 (2018).
- [77] Y. Dubi and Y. Sivan, “hot” electrons in metallic nanostructures—non-thermal carriers or heating?, *Light: Science & Applications* **8**, 89 (2019).
- [78] J. P. Ziegler, James F. and Biersack, The stopping and range of ions in matter, in *Treatise on Heavy-Ion Science*, Vol. 6, edited by D. A. Bromley (Springer US, Boston, MA, 1985) pp. 93–129.
- [79] R. Peierls, Zur kinetischen theorie der wärmeleitung in kristallen, *Annalen der Physik* **395**, 1055 (1929).
- [80] R. E. Peierls, *Quantum theory of solids* (Clarendon Press, 1996).
- [81] M. Simoncelli, N. Marzari, and F. Mauri, Unified the-

- ory of thermal transport in crystals and glasses, *Nature Physics* **15**, 809 (2019).
- [82] M. Simoncelli, N. Marzari, and F. Mauri, Wigner formulation of thermal transport in solids, *Physical Review X* **12**, 041011 (2022).
- [83] E. Di Lucente, M. Simoncelli, and N. Marzari, Crossover from boltzmann to wigner thermal transport in thermoelectric skutterudites, *Physical Review Research* **5**, 033125 (2023).
- [84] A. Cepellotti and N. Marzari, Thermal transport in crystals as a kinetic theory of relaxons, *Physical Review X* **6**, 041013 (2016).
- [85] In particular, Eq. 6 of Ref. [49] encompasses as special cases both thin films and thin wires, as discussed after Eq. 5 of Ref. [67] and Eq. 11.2.9 of Ref. [68].
- [86] Mathematica, *Wolfram Research Inc., Champaign, IL* (Version 12.0, 2019).

SUPPLEMENTARY MATERIAL

Sample preparation

We use commercial (100) CVD single crystalline diamond substrate (Hiqute Diamond, Rouge-T12-100), enriched to above 99.95% in ^{12}C isotopes and containing an NV-rich layer (1–2 ppm) of $\sim 3\ \mu\text{m}$ thickness at the surface. We first perform preliminary acid cleaning: piranha solution ($\text{H}_2\text{SO}_4:\text{H}_2\text{O}_2$ 3:1) and hydrofluoric acid remove organics and metallic residuals, respectively. The substrate is then mounted on a silicon chip with $2\ \mu\text{m}$ thick wet oxide via QuickStick wax. We apply a reported non-contact ion beam polishing method to improve the surface roughness [69].

To define the chromium patches, a 150 nm-thick Cr layer is evaporated on the NV-rich diamond surface. The patches are then defined using electron beam lithography followed by wet etching. 150 nm of hydrogen silsesquioxane (HSQ; XR-1541-006) is spin-coated, written with electron beam lithography, and subsequently developed in tetramethylammonium hydroxide (TMAH 25%) as a mask. TechniEtch Cr01 from MicroChemicals ($(\text{NH}_4)_2\text{Ce}(\text{NO}_3)_6 + \text{HClO}_4$) removes the unmasked Cr layer. Non-contact ion polishing is used to clean the sample surface, and then the patches are released by HF 1%.

We then define the cantilevers, aligned to the Cr patches, using a second round of electron beam lithography followed by several etching steps. A thin titanium layer (40 nm) is evaporated on the surface. A $2\ \mu\text{m}$ -thick layer of HSQ (FOx-16) is spin coated above and exposed with electron beam lithography followed by the aforementioned development process. The Ti layer serves as a conductive and adhesive layer between diamond and HSQ. A Chlorine-based reactive ion etching process is used to pattern the Ti layer (STS Multiplex ICP, 800 W ICP power, 150 W bias power, 10 sccm Cl_2 and 10 sccm BCl_3 , 3 mTorr). To transfer the pattern from the HSQ hard mask to the diamond, a vertical etch is applied with directional oxygen plasma (STS Multiplex ICP, 400 W ICP power, 200 W bias power, 50 sccm O_2 , 15 mTorr). Faraday cage angled etch is then used under the same plasma condition as the previous step to undercut the structures [70]. The hard mask is stripped in the HF 1% bath.

Since the Faraday cage angled etch technique restricts the lateral dimensions of suspended structures, we proceed further with focused ion beam (FIB) milling. This method allows greater flexibility in structuring, enabling us to precisely polish narrow cantilevers and undercut wider ones [71, 72]. A 200 nm Ti layer is deposited to shield the sample from gallium (Ga) implantation and to prevent drift during milling caused by charge accumulation. The milling is conducted with a Zeiss CrossBeam 540 SEM/FIB dual beams system using 30 kV Ga^+ ions on both sides of each cantilever. We apply cross-section mode with 1.5 nA beam current to sputter away most of the material and lower the ion current to 700 pA to realize better sidewall smoothness. Finally, cantilevers with finely polished sidewalls are revealed after removing the Ti layer in HF bath, as shown in Fig. 1b.

Experimental setup

All experiments are carried out in our home-built confocal microscope. The diamond sample is mounted on a temperature-controlled stage, kept at a constant temperature of $22\ ^\circ\text{C}$ for experiments in Fig. 2 and Fig. 3. The output beam of a 515 nm laser is split into two beams, one for heating the chromium patch at the apex of the cantilever and the other one for reading out the NV centers' fluorescence all along the cantilever. The power of each beam can be controlled independently. The two beams are focused on different positions of the cantilevers with a high numerical aperture microscope objective ($\text{NA}=0.9$). The fluorescence is collected into a multi-mode fiber and detected with a multi-pixel photon counter (Hamamatsu C14455-1550GA).

Microwaves are delivered to the sample with a wire loop placed in close vicinity to the diamond sample. The microwave frequency is sinusoidally modulated at 5 kHz by the microwave generator (Rhodes&Schwarz SMB 100A) to be used in combination with the lock-in amplifier. The readout parameters are chosen to optimize temperature sensitivity: the readout laser power is 0.2 mW, the microwave power is 41 dBm and the microwave frequency modulation depth is 5 MHz (corresponding to approximately half of the ODMR linewidth). We have checked that the above parameters do not affect the measured value of the zero-field splitting (ZFS), confirming that the spin readout induces negligible local heating inside the cantilever. We have also verified that the heating laser does not induce any change in ZFS when focused on other portions of the cantilever, away from the metal patch.

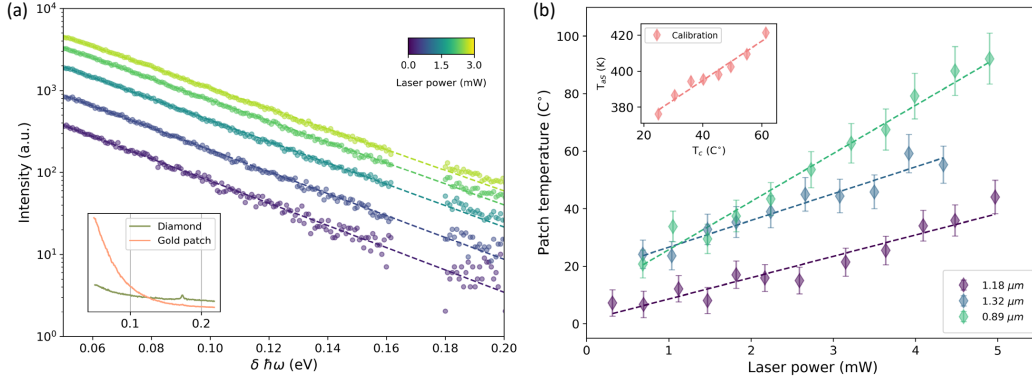


FIG. S1. (a) Anti-Stokes emission spectra of Au patch at the tip of a 1.32 μm -wide cantilever, for different heating laser power. Dashed lines are fit using Eq. (S1), allowing to obtain the temperature of hot carrier T_{aS} . (Inset) Comparison of emission spectra acquired on the diamond cantilever and Au patch, with identical experimental conditions. In the diamond spectrum, a Raman peak appears at $\delta\hbar\omega=0.17$ eV. (b) Extracted patch temperature T_p versus applied heating laser power, measured on three cantilevers with different widths. (Inset) Calibration of T_{aS} as a function of sample base temperature T_c , performed on a large $20\ \mu\text{m} \times 20\ \mu\text{m}$ Au patch on bulk diamond to ensure the patch is at the same temperature as the temperature-controlled stage. Dashed line is a linear fit, used to convert T_{aS} into patch temperature T_p in the main panel.

Independent study of the patch temperature

To confirm that the metal patch is well thermalized with the diamond cantilever, we measure the hot carrier anti-Stokes emission of the patch to get an independent estimate of its temperature. Luminescence in noble metals following photoexcitation is a complex process influenced by various mechanisms, including electron-electron scattering, electron-phonon coupling, multiphoton excitations, and surface plasmons [73, 74]. Anti-Stokes emission corresponds to photons emitted at a higher energy than the energy of the laser incident on the material. As detailed in previous studies, the anti-Stokes emission spectrum can be fit with Boltzmann statistics to obtain a first approximation of the effective temperature [73, 75]. Under the assumption that both the photonic and electronic densities of states vary much slower than the Boltzmann factor close to the laser energy [75, 76], we have the simple expression for the anti-Stokes intensity as a function of the Raman shift $\delta\omega$

$$I_{aS}(\delta\omega) \propto A \exp\left(\frac{-\hbar\delta\omega}{k_B T_{aS}}\right) \quad (\text{S1})$$

from which we can determine the effective temperature T_{aS} .

We measure the anti-Stokes emission spectrum on three different cantilevers, using 532 nm continuous wave excitation and a spectrometer. A notch filter rejects most of the reflected excitation laser. Collected spectra are shown in Fig. S1a and can be well fitted with the exponential decay from Eq. (S1) over the $\delta\omega$ range that we can experimentally access. Note that we discard the energy window corresponding to the Raman peak of diamond, to avoid spurious residual contribution from the diamond cantilever. We extract the anti-Stokes temperature T_{aS} from the fit. This experiment was performed on a patch made of gold (Au) instead of Cr, but with a few nm-thin Cr layer used as adhesion layer between Au and diamond. Hence, aside from the absorption coefficient of the patch α , no major qualitative difference is expected in the metal-to-diamond thermalization efficiency.

The relationship between T_{aS} and the lattice temperature is in general not straightforward, specifically under continuous wave illumination [77]. Hence, we perform a calibration measurement to relate the extracted T_{aS} to the patch temperature, using the temperature-controlled stage on which the diamond sample is mounted (see inset of Fig. S1b). We find that the relation between T_{aS} and the controlled patch temperature T_p can be well described using a linear fit: $T_{aS} = aT_p + b$. We can therefore determine the temperature of metal patches versus heating laser power, on cantilevers with different widths, as shown in Fig. S1b. Although this method does not grant high precision (note also that the extracted zero-laser-power temperature is significantly lower on the 1.18 μm cantilever), this measurement proves that the metal patch temperature increases linearly when heating laser is applied. Temperature estimates with anti-Stokes emission are also found to be of the same order as values presented in the main text on diamond cantilevers for similar heating power, meaning that the interface thermal resistance between the patch and diamond

is sufficiently small. Our main conclusion is that convective and radiative thermal losses from the metal patch to the surrounding can safely be neglected.

Experimental estimate of the effective thermal conductivity

The effective thermal conductivity of our cantilevers is defined as $\kappa_{\text{eff}} = q(dT/dx)^{-1}$. The temperature gradient dT/dx is directly extracted from the measured temperature profile. We only need to estimate the heat flux density q in order to obtain κ_{eff} . As introduced in the main text, we have $q = \alpha P_h/S$. The heating laser power incident on the Cr patch P_h is measured directly. The Cr patch absorption coefficient α is estimated by measuring its reflection coefficient r and assuming negligible transmission and scattering, i.e. $\alpha = 1 - r$. Finally, the cantilever cross-section is $S = \tan(\theta)w^2/4$, where both the width w and cross-section angle θ are estimated from SEM images of the different cantilevers, see for example Fig. 3a of the main text.

We assume an uncertainty of 50 nm in the extracted width w from SEM images. This uncertainty needs to be properly taken into account in the uncertainty of κ_{eff} , together with the uncertainty on the temperature gradient. We find that the width uncertainty is the dominant factor, explaining the significantly bigger error bars in κ_{eff} , see Fig. 4, compared to the temperature gradient in Fig. 3c.

Additional figures

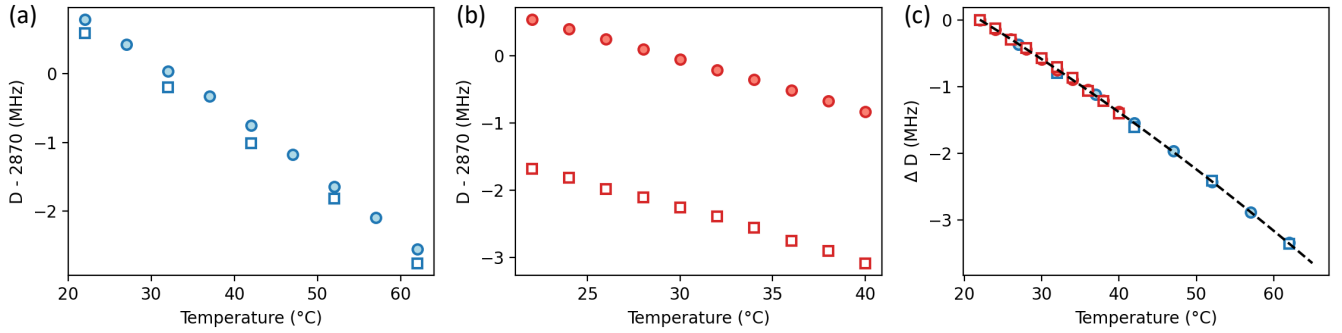


FIG. S2. Detailed temperature calibration data from Fig. 1c. (a, b) Raw ZFS value versus temperature measured in the bulk (circles) and on a cantilever (squares), for (a) sample A: a diamond with natural abundance (i.e. 1.1%) of ^{13}C and low NV concentration of 10 ppb and (b) sample B: a diamond isotopically enriched to above 99.95% ^{12}C and NV concentration of 3 ppm. (c) Corresponding ZFS shift ΔD versus temperature from (a,b), with the same colors and symbols as in (a, b). Note that this data is the same as in Fig. 1c, but the colors clearly differentiate the two diamonds, highlighting that the temperature-induced ZFS shift is largely independent of the diamond hosting the NV centers. Note also that all other measurements presented both in the main text and Supplementary Materials are obtained with the isotopically enriched diamond (sample B). Black dashed line in (c) is a fit with the expression from Ref. [48]: $D(T) = D_0 + c_1 n_1 + c_2 n_2$, with $n_i = 1/(e^{\Delta_i/k_b T} - 1)$ the phonon population in mode i , with energy Δ_i . We use the same two mode energy as in [48], but keep the constants $c_{1,2}$ as fitting parameters (here, $c_1 = -32.6$ MHz and $c_2 = -630$ MHz). Note that the fit gives a linearized temperature shift $dD/dT = -78$ kHz/K around 30 °C, corresponding to the widely reported value in the literature for room temperature.

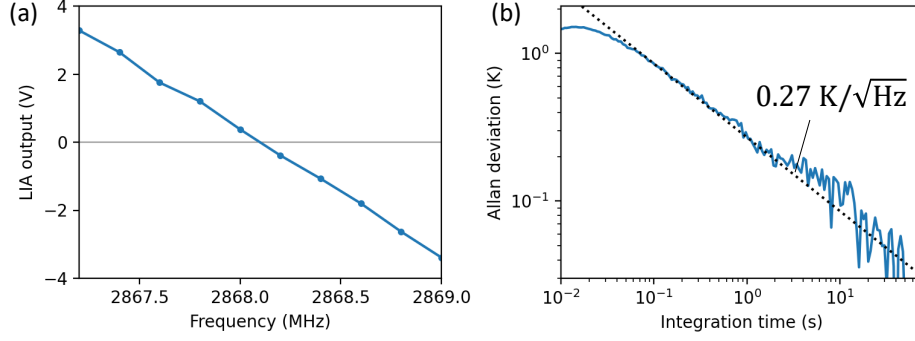


FIG. S3. Estimation of temperature sensitivity. (a) Lock-in ODMR spectrum, measured on a cantilever and at 22°C . Compared to the top inset in Fig. 1c, here the microwave frequency range is limited to values around the NV resonance (i.e. close to the ZFS value). A linear fit gives a slope of $-3.7 \text{ V}/\text{MHz}$, which characterizes the lock-in amplifier (LIA) output response to any ZFS shift. (b) Allan deviation of the LIA output, for the same experimental conditions as in (a) and a central microwave frequency of 2868.0 MHz. The conversion from LIA output noise to temperature noise is done by using the slope extracted from panel (a) and a linear approximation $dD/dT = -78 \text{ kHz}/\text{K}$ (see discussion in the caption of Fig. S2). We get a temperature readout sensitivity of $0.27 \text{ K}\cdot\text{Hz}^{-1/2}$. Note that the integration time in the 10-point spectrum shown in (a) is 3 s per point, yielding a temperature readout accuracy below 0.15 K.

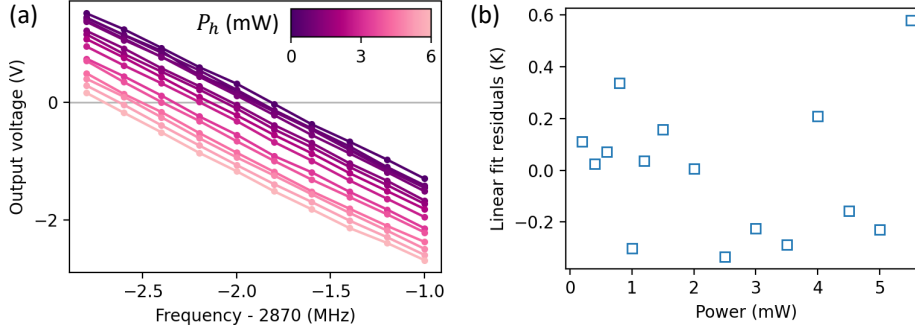


FIG. S4. Detailed power scan data of Fig. 2a. (a) Complete set of LIA ODMR spectra measured for increasing heating power P_h , as indicated by the color of each line. (b) Difference between the measured temperature shift and the linear fit of the power scan from Fig. 2a. The standard deviation of these fit residuals is 0.25 K, corresponding to the temperature accuracy that includes systematic errors due e.g. to imperfect alignment of the heating laser on the Cr patch. It is thus slightly higher than the readout error derived from the Allan deviation in Fig. S3.

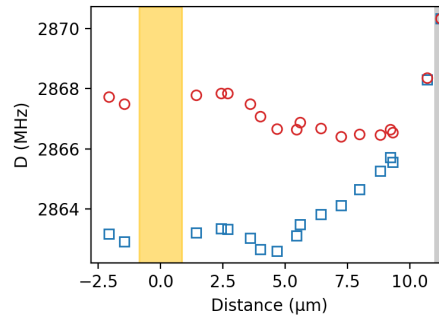


FIG. S5. ZFS profile along the cantilever from Fig. 2b, measured without heating, $P_h = 0$, (red circles) and with heating, $P_h = 3.07 \text{ mW}$ (blue squares). Even in the absence of heating, strong variations of the ZFS along the cantilever are observed, attributed to local strain or stray electric fields caused by surface charges. The corresponding temperature profile shown in Fig. 2c is obtained by subtracting the two measurements, and converting the resulting ΔD to temperature shift ΔT using the calibration from Fig. 1(c).

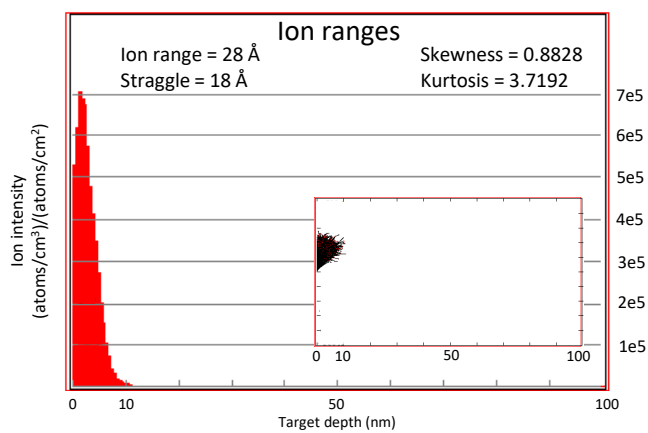


FIG. S6. Monte Carlo simulations of 30 kV gallium ions coming under a polishing angle (1°) to the diamond[78]. The SRIM simulation predicts that the depth of the implantation is of the order of 10 nm. The inset shows the collision plot.

Theoretical analysis

An established approach to describe thermal transport in crystals from first principles is the linearized phonon Boltzmann transport equation (LBTE) [68, 79, 80]:

$$\left. \frac{\partial n_\nu(\mathbf{r}, t)}{\partial t} + \mathbf{v}_\nu \cdot \frac{\partial n_\nu(\mathbf{r}, t)}{\partial \mathbf{r}} = \frac{\partial n_\nu(\mathbf{r}, t)}{\partial t} \right|_{\text{col.}}, \quad (\text{S2})$$

where n_ν is phonon distribution ($\nu \equiv \mathbf{q}s$, with \mathbf{q} being the phonon wavevector and s the phonon mode index). The LBTE is a microscopic model, which describes the propagation and scattering of phonons in the presence of a temperature gradient. The LBTE can be parametrized from first principles, and its linear-response solution allows to predict the thermal conductivity. We note, in passing, that the LBTE has been recently generalized to account not only for the ability of phonons to propagate particle-like, but also for their capability to tunnel wave-like [81–83]. In diamond, propagation dominates over tunneling and the LBTE accurately describes thermal transport [14].

The first-principles solution of the LBTE has the drawback of being computationally expensive, making it unpractical to explore how nanostructure shape affects heat transport. Therefore, to investigate thermal transport in cantilevers having different cross-section shapes and sizes, we rely on the mesoscopic viscous heat equations (VHE) [14]. The VHE are two coupled partial differential equations for the mesoscopic temperature (T) and phonon drift-velocity (\mathbf{u}) fields. They are obtained from coarse-graining the LBTE [14, 84]. The VTE encompass both the diffusive (Fourier) and hydrodynamic regimes [7, 84] of thermal transport, as well as the crossover between them. It has been shown that the VHE rationalizes the experimental demonstration of hydrodynamic transport in graphite [14], and also yields predictions compatible with the space-dependent solution of the LBTE [57, 58] in complex-shaped devices [59]. In the steady-state regime, for a material with isotropic transport properties such as diamond, the VHE read:

$$\begin{cases} \alpha \nabla \cdot \mathbf{u}(\mathbf{R}) = \kappa \nabla^2 T(\mathbf{R}) \\ \beta \nabla T(\mathbf{R}) - \mu \nabla^2 \mathbf{u}(\mathbf{R}) = -\gamma \mathbf{u}(\mathbf{R}), \end{cases} \quad (\text{S3})$$

where μ is the phonon viscosity, the coupling coefficients α and β arise from the energy-crystal momentum relation for phonons [14], while γ accounts for the presence of momentum-dissipating scattering processes [14]. We use capital \mathbf{R} to emphasize the space variation at the mesoscopic scale.

From Eq. (S3) one can derive energy and momentum balance equations in terms of a heat flux generalized to the hydrodynamic regime:

$$Q_i(\mathbf{R}) = -\kappa \sum_j \frac{\partial T(\mathbf{R})}{\partial R_j} + \alpha \sum_j u_j(\mathbf{R}), \quad (\text{S4})$$

where i labels Cartesian directions.

The mesoscopic heat flux is then used to evaluate the effective thermal conductivity across the cantilevers. For a cantilever, taken along x axis, of length L and with an imposed temperature difference at its boundaries ΔT , we get:

$$\kappa_{\text{eff}} = \bar{q} \frac{L}{\Delta T}, \quad (\text{S5})$$

where $\bar{q} = S^{-1} \iint_S \mathbf{q} \cdot d\mathbf{S}$ is the average heat flux discussed in the main text.

In the limit of negligible hydrodynamic effects, Eqs. (S3) reduce to the Fourier's law of diffusive heat conduction:

$$-\kappa \nabla^2 T(\mathbf{R}) = 0. \quad (\text{S6})$$

In this regime the heat flux simply becomes

$$Q_i(\mathbf{R}) = -\kappa \sum_j \frac{\partial T(\mathbf{R})}{\partial R_j}, \quad (\text{S7})$$

The importance of viscous effects can thus be estimated by comparing the results of computing the heat flux with Eq. (S4) (full solution) versus Eq. (S7) (purely diffusive case).

All the parameters entering the VHE can be determined from the first-principles solution of the full LBTE (*i.e.* accounting for the actual phonon band structure and full collision matrix). An exact solution of the LBTE has been discussed for the case of nanowires [49, 60] under the assumption of diffusive boundaries. This approach allows to

account for the influence of boundary scattering on the conductivity of wires, providing an expression which depends only on the cross-section of the wire [85] and can be applied to the triangular cross-section nanowire studied in this work. After verifying with the established Casimir model [50] that boundary scattering has strong effects on the conductivity but has negligible effect on the other parameters entering the VHE (including the thermal viscosity μ), we accounted for nanowire boundary scattering on the conductivity only and used bulk values (calculated in Ref. [14]) for the other parameters entering in the VHE. This approximation is further justified a posteriori, since Fig. 4 shows that viscous effects are unimportant in the cases considered here.

Finally, we discuss how we considered the Ga contamination in the vicinity of milled faces of the cantilevers (i.e. bottom faces, see inset of Fig. 4). Since with the methods currently available it is not possible to solve the LBTE with position-dependent Ga content, we consider uniform Ga impurities over the whole cantilever cross-section. This approximation allows to capture the increased relative influence of the Ga-contaminated layer (of fixed depth $d = 0.01\mu\text{m}$, see main text) when reducing the cantilever width w . In particular, we consider an impurity concentration proportional to the ratio of contaminated area to total cross-section area, referred to as penetration ratio PR

$$\text{PR}(w) = \frac{S_{\text{Ga}}}{S} \simeq \frac{d}{w} \frac{4}{\sin\theta}, \quad (\text{S8})$$

where the approximated equality holds at linear order in d/w ; details on the geometrical analysis performed to compute $\text{PR}(w)$ are reported in the next section. Eq. (S8) allows us to describe the width-dependent average Ga concentration $\eta(w)$ as:

$$\eta(w) = \eta_{\text{Ga}} \text{PR}(w), \quad (\text{S9})$$

where η_{Ga} is the concentration of Ga impurities in the contaminated layer. We thus determine the conductivity from the linear-response solution of the LBTE, accounting for phonon-impurity scattering with impurity strength parameter corresponding to Ga impurities with concentration $\eta(w)$ [61].

In summary, we determine the linear-response solution of the LBTE (Eq. (S2)) for diamond nanowires with width-dependent Ga impurity scattering using the **ShengBTE** package [60] and use the bulk thermal viscosity computed following the theoretical prescriptions of Ref. [14]. Then, we solve the VHE numerically (Eq. (S3)) using a finite-element solver implemented in Mathematica [86], imposing a temperature gradient $\Delta T = 10$ K around room temperature on $L = 10\mu\text{m}$ long cantilevers. Finally, we obtain the effective thermal conductivity from Eqs (S4) and (S5). The Ga concentration in the contaminated areas η_{Ga} is set in the **ShengBTE** simulation so as to fit the experimental trend of κ_{eff} vs width (black squares in Fig. 4 of the main text). This is the sole fitting parameter in our model.

Evaluation of the Ga participation ratio

Given that Ga impurities are mostly localized on the two slanted sides of Diamond cantilevers (see inset of Fig. 4), we can compute the participation ratio, PR, as the ratio between the azure area in the triangle on the right of Fig. 4, S_{Ga} , to the total triangular section, $S_{\text{tot.}}$. Considering an angle at the surface equal to 53° , with some algebra one finds

$$S_{\text{Ga}} = 2 \frac{d \left[\frac{w}{\cos(53^\circ)} - d \left(1 + \frac{1}{\tan(53^\circ)} \right) \right]}{2}, \quad (\text{S10})$$

where the fraction multiplied by a factor of 2 represents each of the d -deep areas related to the two slanted sides (see the inset of Fig. 4 of the main text). On the other hand, the total triangular section is simply

$$S_{\text{tot.}} = \frac{w^2}{4} \tan(53^\circ). \quad (\text{S11})$$

These considerations allow us to approximate $\text{PR}_d(w)$ to linear order in d/w and justify Eq. (S8) as shown below:

$$\begin{aligned} \text{PR}_d(w) &= \frac{S_{\text{Ga}}(w, d)}{S_{\text{tot.}}(w)} = \\ &= \frac{d}{w} \frac{4}{\sin(53^\circ)} - \frac{d^2}{w^2} \left(\frac{4}{\tan(53^\circ)} + \frac{4}{\tan^2(53^\circ)} \right) \simeq \\ &\simeq \frac{d}{w} \frac{4}{\sin(53^\circ)}. \end{aligned} \quad (\text{S12})$$

The solution of the LBTE with a space-dependent scattering term for nanowires is obtained using the ShengBTE package. Even if the solution is valid for any cross-section shape (it depends only on the cross-section value), the ShengBTE implementation is coded assuming a circular cross-section. So, the widths of the prismatic cantilevers are obtained from the ShengBTE simulations by matching circular cross-section used in the simulation, $S_{\text{circle}} = \pi r^2$ (r being the radius of the cylindrical nanowire simulated), with the triangular cross-section, $S_{\text{triangle}} = \frac{w^2}{4} \tan(53^\circ)$. This simply translates into getting the width values of triangular nanowires (used on the x axis of Fig. 4 of the main text) as $w = 2\sqrt{S_{\text{circle}} \cot(53^\circ)}$.

Finally, in Fig. S7, we show further effective thermal conductivity calculations obtained using a fixed (non width-resolved) Ga-impurity concentration. We clearly observe that the slope of such curves does not capture the experimental trend, highlighting the necessity to consider a Ga-impurity model.

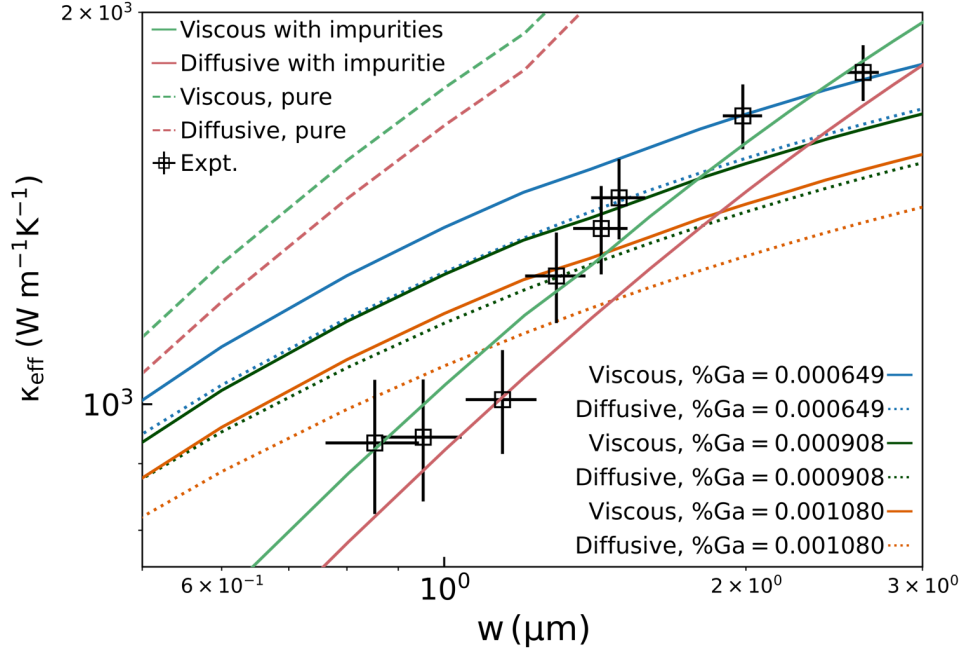


FIG. S7. Effective thermal conductivity of diamond cantilevers as a function of their width w . Blue, dark green and orange are simulations with fixed Ga-impurity concentration equal to 0.000649%, 0.000908% and 0.001080%, respectively; solid lines are first-principles predictions based on the viscous heat equations, dotted lines are predictions from Fourier's law. The other data are the same reported in Fig. 4: black squares are experiments; light green (red) are first-principles predictions based on the viscous heat equations (Fourier's law), with solid style accounting for Ga impurity proportional to the surface-to-volume ratio, while the lines with dashed style consider impurity scattering only from carbon isotopes (0.05% of ^{13}C).